Distribution of aseismic slip rate on the Hayward fault inferred from seismic and geodetic data

D. A. Schmidt
Department of Geological Sciences, University of Oregon, Eugene, Oregon, USA

R. Bürgmann and R. M. Nadeau
Berkeley Seismological Laboratory, University of California Berkeley, Berkeley, California, USA

M. d'Alessio
U.S. Geological Survey, Menlo Park, California, USA

Received 20 August 2004; revised 24 April 2005; accepted 16 May 2005; published 16 August 2005.

[1] We solve for the slip rate distribution on the Hayward fault by performing a least squares inversion of geodetic and seismic data sets. Our analysis focuses on the northern 60 km of the fault. Interferometric synthetic aperture radar (InSAR) data from 13 independent ERS interferograms are stacked to obtain range change rates from 1992 to 2000. Horizontal surface displacement rates at 141 bench marks are measured using GPS from 1994 to 2003. Surface creep observations and estimates of deep slip rates determined from characteristic repeating earthquake sequences are also incorporated in the inversion. The fault is discretized into 283 triangular dislocation elements that approximate the nonplanar attributes of the fault surface. South of the city of Hayward, a steeply, east dipping fault geometry accommodates the divergence of the surface trace and the microseismicity at depth. The inferred slip rate distribution is consistent with a fault that creeps aseismically at a rate of ~5 mm/yr to a depth of 4–6 km. The interferometric synthetic aperture radar (InSAR) data require an aseismic slip rate that approaches the geologic slip rate on the northernmost fault segment beneath Point Pinole, although the InSAR data might be complicated by a small dip-slip component at this location. A low slip rate patch of <1 mm/yr is inferred beneath San Leandro consistent with the source location of the 1868 earthquake. We calculate that the entire fault is accumulating a slip rate deficit equivalent to a $M_w = 6.77 \pm 0.05$ per century. However, this estimate of potential coseismic moment represents an upper bound because we do not know how much of the accumulated strain will be released through aseismic processes such as afterslip.

Citation: Schmidt, D. A., R. Bürgmann, R. M. Nadeau, and M. d'Alessio (2005), Distribution of aseismic slip rate on the Hayward fault inferred from seismic and geodetic data, *J. Geophys. Res.*, *110*, B08406, doi:10.1029/2004JB003397.

1. Introduction

[2] Several faults within the San Andreas fault system have long been known to exhibit interseismic creep at the surface, including the central San Andreas fault, the Maacama fault, the Concord fault, the Calaveras fault, and the Hayward fault [*Galehouse*, 2002]. Historically, fault creep was believed to be limited to the shallow subsurface where the stresses are low, except on the central San Andreas fault where creep is believed to extend to seismogenic depths [*Wesson*, 1988]. More recent observations have revealed that the range of faulting behavior is not limited to steady, interseismic creep or coseismic rupture, but rather that these represent end-members. The detection of slow earthquakes along subduction zones [*Dragert et al.*, 2001; *Miller et al.*, 2002], transient aseismic slip events on the central San Andreas fault [*Linde et al.*, 1996], and postseismic afterslip [*Smith and Wyss*, 1968; *Bilham*, 1989; *Bürgmann et al.*, 2002] have demonstrated a richer spectrum of faulting behavior than was previously appreciated.

[3] The Hayward fault in the San Francisco Bay Area presents itself as a candidate system for the study of aseismic fault behavior because a wide range of complementary data sets are readily available. The Hayward fault is a major strand of the San Andreas fault system accommodating nearly 25% of the deformation (Figure 1). The fault exhibits a diversity of slip behaviors including large coseismic rupture (a *M*6.8 in 1868), frequent microseismicity, and aseismic creep. Surface creep is observed along the entire length of the fault in the range of 3–9 mm/yr and the rates appear to be consistent over the past several decades

0148-0227/05/2004JB003397$09.00

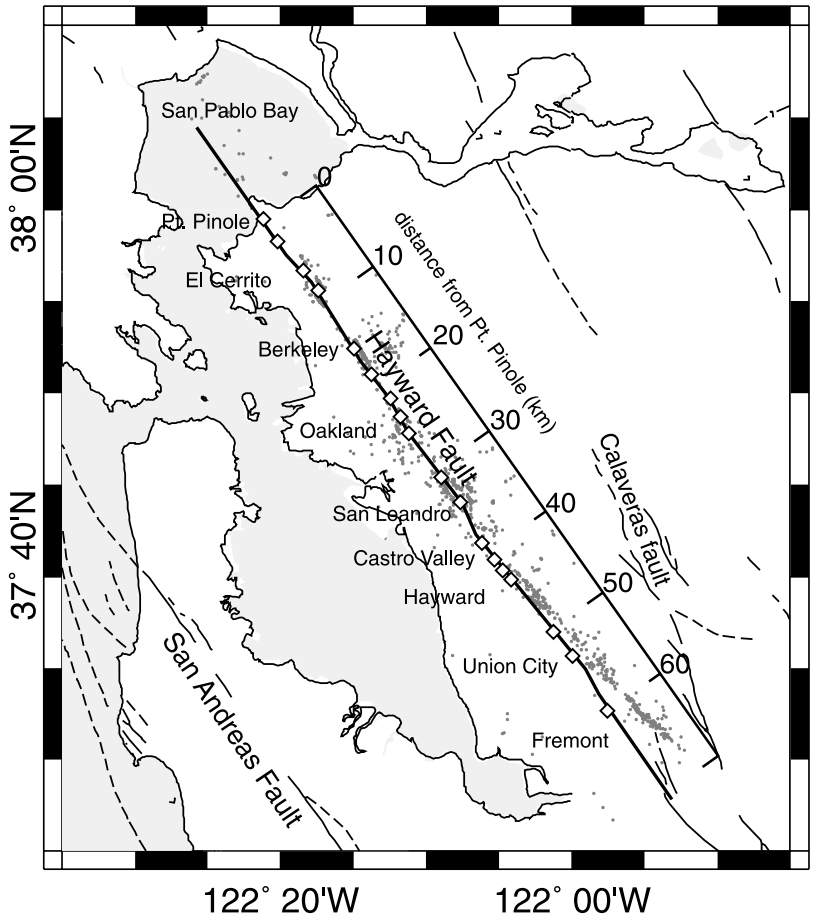

Figure 1. Map of the major faults the San Francisco Bay Area in the region including the San Andreas, Hayward, Calaveras, and Greenville faults. The surface trace of the modeled Hayward fault is shown with a bold line. The background seismicity (gray dots) and the location of surface creep observations (solid squares) are also shown. The scale bar marks the distance along the fault from Point Pinole.

[*Lienkaemper and Galehouse*, 1997]. The geologic slip rate on the fault is estimated at ~9 mm/yr [*Lienkaemper and Borchardt*, 1996; *Lienkaemper et al.*, 1991; *Williams*, 1995]. The difference between the geologic and contemporary creep rates suggests that a slip deficit exists, and that the accumulating elastic strain will presumably be released in future earthquakes.

[4] Assessing the seismic potential and developing our understanding of the fault has been the topic of several previous studies. The established model for the Hayward fault consists of a fault that is locked from a depth of 3–5 km to the bottom of the seismogenic zone (~12 km). The upper portion of the fault exhibits aseismic creep that is driven by plate boundary forces. *Savage and Lisowski* [1993] developed a friction model to relate the depth of creep and the rate of stress accumulation to the surface creep rate. They estimate that strain is accumulating at a rate equivalent to a *M*6.8 event per century for the entire length of the fault. *Lienkaemper and Galehouse* [1998] upgraded the seismic potential of the fault to ~*M*7 based on a larger fault area. Using space geodetic data, *Bürgmann et al.* [2000] inverted directly for the depth of creep on the northern segment of the Hayward fault and found that 7 mm/yr of aseismic slip at depth was required. The lack of significant locking at depth north of Berkeley can be reconciled with the observed surface creep distribution in a mechanical model of a freely slipping northern Hayward fault driven by slip on deep extensions of the major strike-slip faults, if the fault is locked just north of Point Pinole and locked below 2 km depth south of Berkeley [*Bürgmann et al.*, 2000]. *Simpson et al.* [2001] used a similar elastic boundary element modeling approach to relate the along-strike variation in the surface creep rate to the optimal locking depth along the fault. They identify several regions where the fault is likely locked at depth. *Malservisi et al.* [2003] used a viscoelastic finite element model driven by far-field plate velocities to provide a more realistic representation of the loading conditions on the Hayward fault. Through a series of forward models, they find creep to extend to greater depths than that predicted using elastic models driven by slip on deep dislocations. By analyzing the microseismicity on the fault, *Wyss* [2001] mapped the location of locked asperities using the local recurrence time. *Waldhauser and Ellsworth* [2002] also attempt to identify regions where aseismic slip is restrained, or the fault is locked, based on the distribution of the background

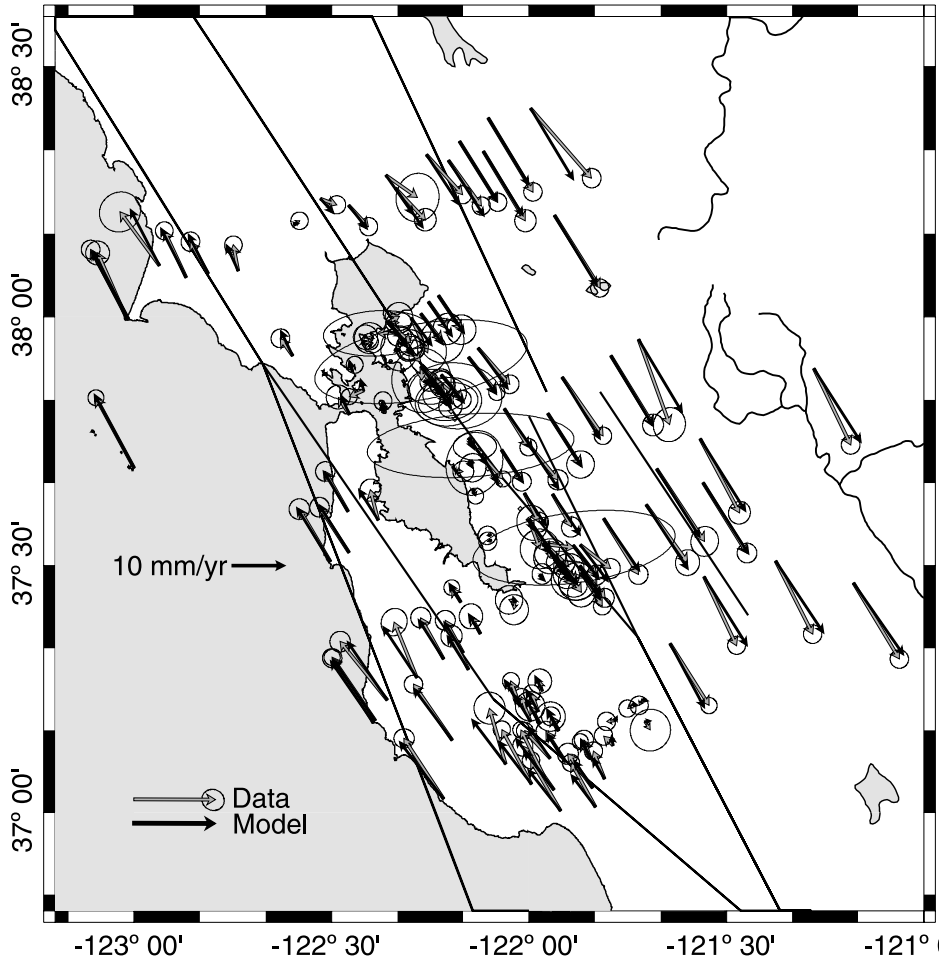

Figure 2. GPS displacement rates (gray arrows) observed from 1994 to 2003 with 2-sigma error ellipses. The predicted surface displacement rates (black arrows) are shown for the slip rate distribution in Figure 7b.

seismicity which they relocate using cross-correlation techniques.

[5] The most significant earthquake to occur on the Hayward fault in historic times was a M6.8 event in 1868 [*Lienkaemper et al.*, 1991; *Toppozada and Borchardt*, 1998]. The event ruptured the southern portion of the fault and extended as far north as Berkeley (at km 20, distance south of Point Pinole along the Hayward fault) [*Yu and Segall*, 1996; *Lawson*, 1908]. No earthquake greater than $\sim M_L$4.5 has been observed on the Hayward fault since seismic instrumentation was installed in the early twentieth century [*Oppenheimer et al.*, 1992]. Paleoseismic data suggest that several large earthquakes have produced surface rupture on both the northern and southern portions of the Hayward fault [*Hayward Fault Paleoearthquake Group*, 1999; *Lienkaemper and Williams*, 1999]. The lack of significant seismic moment release on the northern segment of the fault within recorded history has raised concern that this segment may be overdue for a large earthquake. The *Working Group on California Earthquake Probabilities* [2003] identified the Hayward fault as a significant threat to life and property in California. The hazard associated with such an event is especially significant because the Hayward fault passes beneath several urban communities in the San Francisco Bay Area.

[6] In this paper, the analysis of *Bürgmann et al.* [2000] is greatly expanded to incorporate updated geodetic and seismic data sets and extend the modeling over the northern 60 km of the fault. An inversion for the aseismic slip rate distribution is performed using data from interferometric synthetic aperture radar (InSAR), the Global Positioning System (GPS), slip rate estimates from characteristic repeating earthquake (CRE) sequences, and surface creep rate observations. The inversion results provide evidence for a heterogeneous subsurface slip rate distribution consisting of locked and creeping patches.

2. Data Analysis

2.1. GPS Data Set

[7] Surface displacements are measured using GPS from continuous stations maintained by the BARD network and campaign data collected by the U.S. Geological Survey and University of California Berkeley from 1994 to 2003 (Figure 2). A full description and analysis of the GPS data can be found in *d'Alessio et al.* [2005]. GPS data are

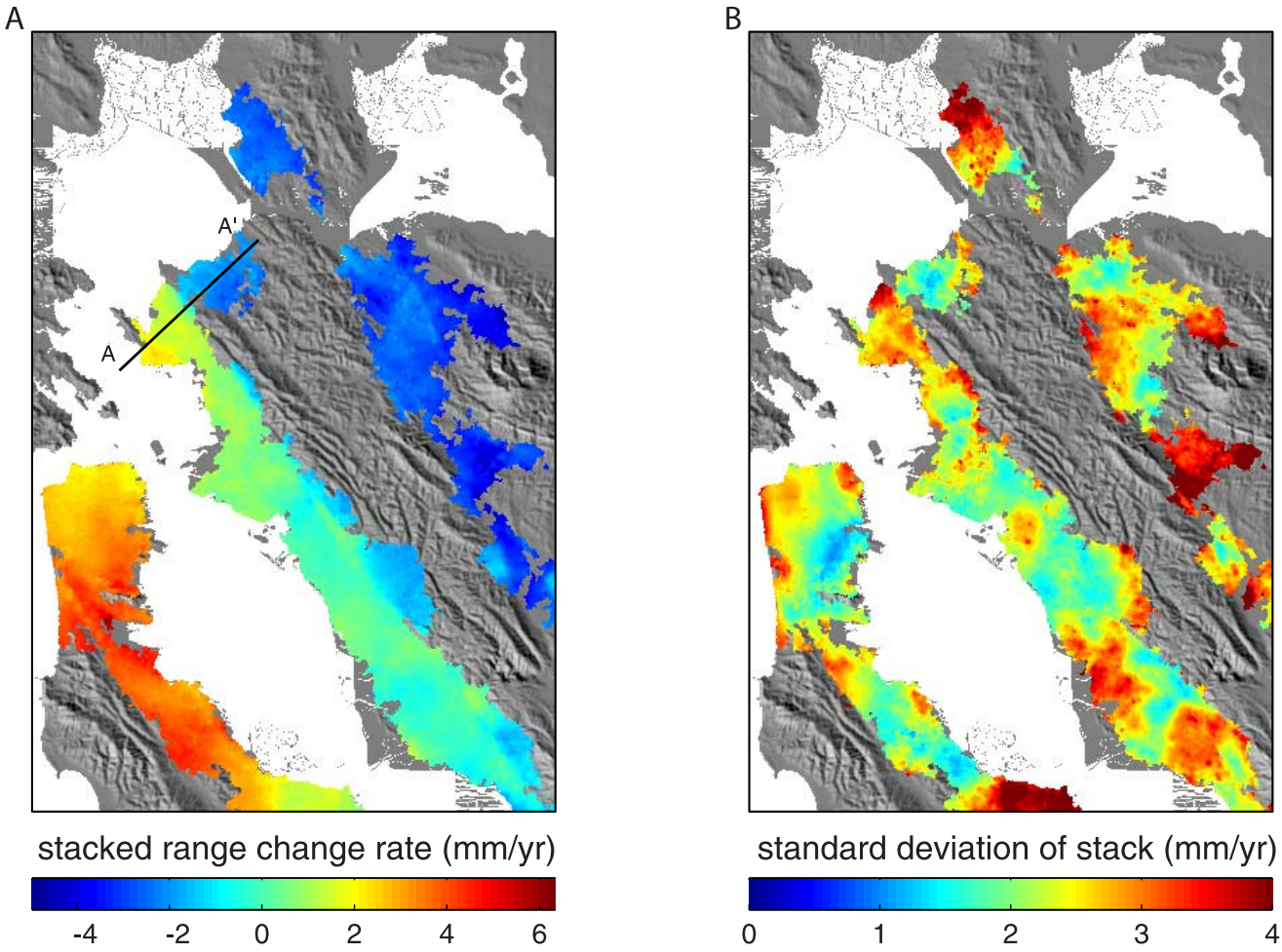

Figure 3. A linear range change rate determined from 13 independent interferograms in the Bay Area from 1992 to 2000. A shaded relief map is shown in the background. InSAR coherence is limited primarily to developed regions for interferograms longer than a few months. The InSAR stack is provided in the auxiliary material.

processed using the Gamit processing package [*Herring*, 2002; *King and Bock*, 2002]. The largest errors in the GPS data are found at campaign sites located along the fault trace which were added to the GPS network beginning in 1997. These sites correspond to the same bench marks used by *Lienkaemper et al.* [2001] to estimate the surface creep rates. The inversion utilizes the horizontal components from 141 stations.

2.2. InSAR Data Set

[8] InSAR data provide a spatially continuous sampling of the deformation field along the line of sight from the satellite. Interferograms are produced using the Repeat Orbit Interferometry Package (ROI PAC) developed at JPL/Caltech. SAR data collected by the ERS-1/-2 satellite of the European Space Agency are processed using 8 looks in range and 40 looks in azimuth resulting in a pixel dimension of 150 m. Range change attributed to topography is removed using a 30-m USGS digital elevation model. A dislocation model constrained by the GPS data is used to remove the interseismic gradient from each interferogram. Any remaining linear gradient, attributed to orbital errors, is removed and the interseismic signal is added back. The magnitude of the interseismic gradient is inconsequential in the inversion in that three model parameters are included that solve for the best fitting regional tilt and offset when fitting the InSAR data. Coherent InSAR data is limited to urban regions located primarily on the west side of the Hayward fault (Figure 3a). Coverage extends across the fault in Pinole (km 0–5), Castro Valley (km 38–44), and Fremont (km 58–65).

[9] A range change rate is calculated by stacking a set of 13 independent interferograms. A full description of the process used to select the interferograms and the subsampling procedure can be found in Appendix A. The list of the interferograms used in this analysis is presented in Table 1. The average temporal baseline of the selected interferograms is 2.9 years, with the longest being 7 years. The relative uncertainties are included in the weighted inversion by constructing a covariance matrix with the diagonal elements equal to the squared standard deviation of each pixel. Data are therefore down-weighted where the standard deviation is relatively large, reflecting a potential bias from atmospheric artifacts or time-dependent deformation (such as seasonal land subsidence) contained in one or more interferograms (Figure 3b). The individual SAR scenes

Table 1. List of Descending Interferograms Used in the Final Stack[a]

Date 1	Date 2	Satellite 1	Orbit 1	Satellite 2	Orbit 2	Perpendicular Baseline, m	Δt, years
19920610	19971011	ERS-1	4724	ERS-2	12950	3	5.3
19920923	19991016	ERS-1	6227	ERS-2	23471	100	7.0
19951110	19970906	ERS-1	22603	ERS-2	12449	40	1.8
19960329	19991120	ERS-1	24607	ERS-2	23972	89	3.6
19960503	19981031	ERS-1	25108	ERS-2	18461	53	2.5
19960504	19990529	ERS-2	5435	ERS-2	21467	36	3.0
19961026	19990213	ERS-2	7940	ERS-2	19964	80	2.3
19970104	20000408	ERS-2	8942	ERS-2	25976	92	3.3
19970802	20000129	ERS-2	11948	ERS-2	24974	30	2.5
19970906	19991225	ERS-2	12449	ERS-2	24473	75	2.3
19971220	19990320	ERS-2	13952	ERS-2	20465	67	1.2
19980509	19990807	ERS-2	15956	ERS-2	22469	25	1.2
19980718	19990911	ERS-2	16958	ERS-2	22970	84	1.1

[a]SAR data were collected by the ERS-1/2 spacecraft along track 70, frames 2835/2853. Dates are in year, month, day.

used to make the 13 interferograms are generally distributed evenly over all of the seasons, except for a slight bias toward spring-to-fall pairs. This helps to avoid strong seasonal signals as might be observed in winter-to-summer pairs. Data on the west side of the fault near San Leandro (km 28–34) are excluded in the inversion because the localized deformation is believed to reflect groundwater-induced deformation of a Pliocene basin [*Marlow et al.*, 1999] (Figure 3). While we have excluded data that appear to be compromised, it is difficult to discern a clear boundary to groundwater-induced deformation. When modeling the InSAR stack, the unit vector used to project the 3-D surface displacements onto the satellite's line of sight is varied across the SAR scene given that the look angle ranges from 20° to 26°.

2.3. Surface Creep Rates

[10] Surface creep rates are obtained from alinement array measurements along the Hayward fault (Figure 4c) [*Lienkaemper et al.*, 1991; *Lienkaemper and Galehouse*, 1997]. The average creep rate along the fault is 5 mm/yr with a distinctive low near Oakland (km 20–30) and anomalous high of 9 mm/yr (pre-Loma Prieta earthquake rate) south of Fremont (km 65–70). Five creep meters are also located along the fault [*Bilham and Whitehead*, 1997]. The three creep meters located north of Fremont all exhibit quasi-constant creep rates. Updated rates averaged over 5 to 30 years of data at 18 sites measured by *Lienkaemper et al.* [2001] are used in the inversion (Table 2).

2.4. Seismic Repeater Rates

[11] Characteristic repeating earthquakes (CREs) are small magnitude events ($\sim M1-2$) with regular recurrence intervals and identical event locations. These event sequences have waveforms with high cross-correlation values (generally >0.95). *Nadeau et al.* [1995] first identified the existence of numerous CREs along the San Andreas fault near Parkfield. *Nadeau and Johnson* [1998] interpreted these events to represent small asperities that are loaded by creep on adjacent portions of the fault. One of the implications of this model is that a relatively large moment release for a small asperity size suggests a high stress drop. *Sammis and Rice* [2001] argue that these events may not represent small strong asperities, but rather outline the boundary between locked and creeping regions. However, CREs have been shown to be widely distributed in regions devoid of locked boundaries [*Nadeau and McEvilly*, 2004]. An alternative explanation was also proposed by *Beeler et al.* [2001] where the asperity undergoes both coseismic and aseismic slip.

[12] *Nadeau and McEvilly* [1999] developed an empirical relationship from the seismic data set in Parkfield to estimate the slip rate at the event location based on the seismic moment release. This technique has successfully been applied to other regions, including the central San Andreas [*Nadeau and McEvilly*, 2004], the Calaveras fault [*Templeton et al.*, 2001], the subduction zone in Japan [*Igarashi et al.*, 2003], and Taiwan [*Chen and Rau*, 2003]. In these areas the repeating earthquake slip estimates are consistent with available geodetic estimates. CREs have also been identified on the Hayward fault and are used to infer the slip rate at depth [*Bürgmann et al.*, 2000]. Regardless of the slip rates estimated using this technique, the presence of the CRE sequences implies that nearby regions of the fault are creeping aseismically and that deep sections of the Hayward fault are not fully locked.

[13] For the present study, we have more than doubled the CRE data set presented by *Bürgmann et al.* [2000] by extending our analysis through time and along the entire length of the fault (Figure 4a). We analyze waveform data from the Northern California Seismic Network from January 1984 to July 2002 and estimate the slip rate at depth using the technique outlined by *Nadeau and McEvilly* [1999] and the empirical parameters used by *Bürgmann et al.* [2000]. The majority of the repeating sequences along the Hayward fault contain only one or two repeat intervals resulting in relatively large 2-sigma uncertainties for some slip rate estimates. For the subsequent inversions, we use slip rate estimates from 95 CRE sequences as an additional data constraint on the slip rate distribution (CRE data provided as auxiliary material[1]).

3. Modeling Procedure

[14] GPS and InSAR data are inverted for the slip rate on dislocations in an elastic half-space using the boundary element code Poly3D [*Thomas*, 1993]. A mesh of triangular

[1]Auxiliary material is available at ftp://ftp.agu.org/apend/jb/2004JB003397.

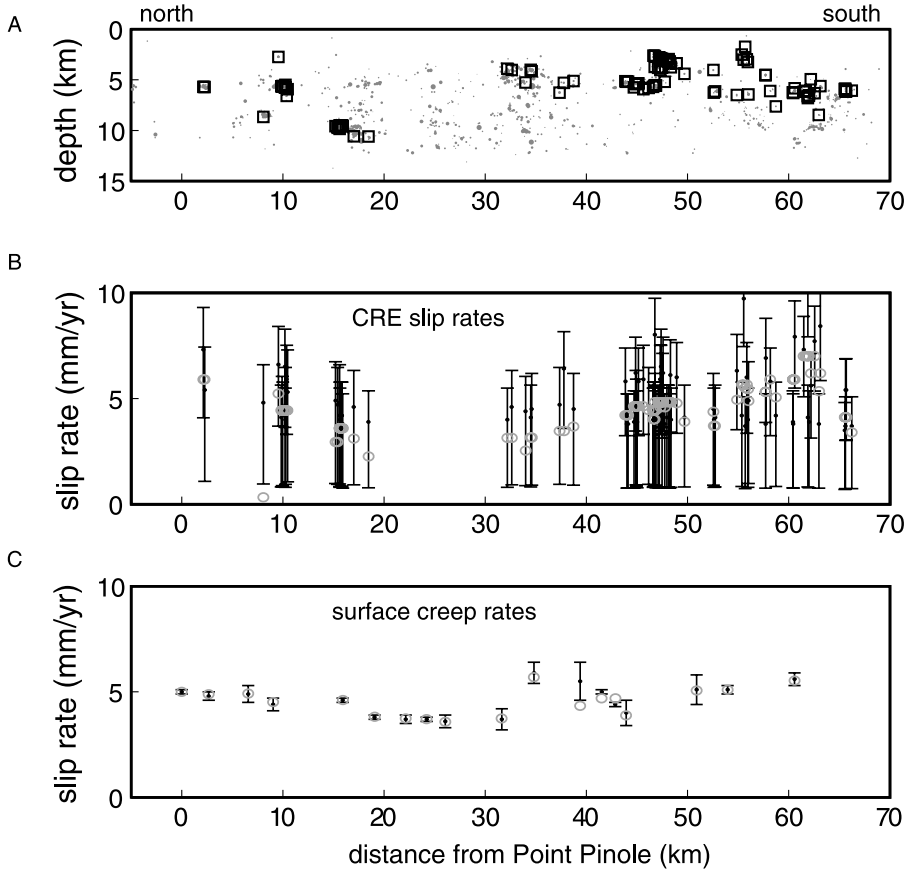

Figure 4. (a) Relocated seismicity (gray dots) of *Waldhauser and Ellsworth* [2002] projected onto the Hayward fault. Characteristic repeating earthquake (CRE) sequences are clustered beneath El Cerrito (km 10), Berkeley (km 18), and San Leandro (km 33) (open squares). (b) Slip rates inferred from the CRE sequences plotted with their 2-sigma uncertainties (black dots with error bars). The slip rates are compared to model results (gray open circles) for the slip rate distribution in Figure 7b. (c) Surface creep rate measurements (black dots with error bars) collected by *Lienkaemper et al.* [2001] displayed according to their location along the Hayward fault. Model results (gray open circles) correspond to the slip rate distribution of Figure 7b.

fault elements, based on the formulation of *Comninou and Dundurs* [1975], allows for a more complex fault geometry than the commonly used rectangular dislocation [*Okada*, 1985]. Surface creep rates and creep rates determined from characteristic repeating microearthquake sequences are used as additional constraints in the inversion. The deformation rate is assumed to be constant over the time spanned by the various data sets. While evidence for episodic aseismic transients have become more common with an increase in observational data and the greater scrutiny of the data sets, surface creep rates appear constant along the northern portion of the fault [*Lienkaemper and Galehouse*, 1997]. Only the southern most few kilometers of the Hayward fault (km 63–68) exhibit transient behavior which appears to be related to the stress perturbation and recovery imposed by the 1989 Loma Prieta earthquake [*Lienkaemper et al.*, 1997; *Schmidt*, 2002]. In this work, the analysis focuses on the Hayward fault north of Union City (km 0–50) where the creep rates appear constant in time.

[15] We compute models of the aseismic slip at depth using linear least squares inversion methods to find a slip rate distribution that minimizes the misfit to the data, while

Table 2. Surface Creep Data Measured at Alignment Arrays by *Lienkaemper et al.*'s [2001], "Best" Rate Using Linear Regression and Predicted Rates From the Model Shown in Figure 7b

Longitude	Latitude	Creep Rate, mm/yr	Model, mm/yr
−122.3546	37.9891	5.0 ± 0.1	5.0
−122.3379	37.9690	4.8 ± 0.2	4.9
−122.3083	37.9425	4.9 ± 0.4	4.9
−122.2918	37.9246	4.4 ± 0.3	4.5
−122.2506	37.8719	4.6 ± 0.1	4.6
−122.2304	37.8484	3.8 ± 0.1	3.8
−122.2090	37.8264	3.7 ± 0.2	3.7
−122.1975	37.8101	3.7 ± 0.1	3.7
−122.1882	37.7951	3.6 ± 0.3	3.6
−122.1504	37.7546	3.7 ± 0.5	3.7
−122.1285	37.7319	5.9 ± 0.5	5.7
−122.1045	37.6950	5.5 ± 0.9	4.3
−122.0899	37.6798	5.0 ± 0.1	4.7
−122.0804	37.6703	4.4 ± 0.1	4.7
−122.0727	37.6627	4.0 ± 0.6	3.9
−122.0222	37.6143	5.1 ± 0.7	5.1
−122.0008	37.5925	5.1 ± 0.2	5.1
−121.9607	37.5422	5.6 ± 0.3	5.5

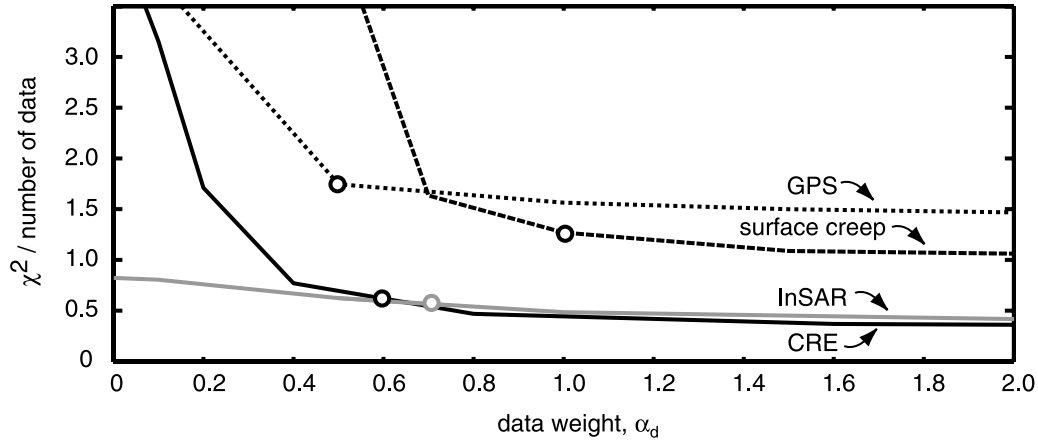

Figure 5. Determination of data weights in a combined inversion of GPS, InSAR, surface creep, and CRE slip rate data. While holding the weight of three data sets fixed to the preferred weight (open circles), the misfit to the fourth data set decreases as the weight is increased as measured by the χ^2 divided by the number of data. The preferred weight is chosen when the data are adequately fit. We observe minimal degradation in fit (<2% increase in χ^2) among the other three data sets when the weight of the fourth is increased.

preserving smoothness of the slip distribution. The weighted inversion minimizes the L2 norm $\|\alpha_d W(d - Gm)\|_2 + \|\gamma\nabla^2 m\|_2$ where m is the strike-slip component on each subfault, G is the design matrix which contains the displacement Green's functions, and d is the data. We use the bounded variable least squares (BVLS) algorithm of *Stark and Parker* [1995] to impose bounds (i.e., positivity and an upper bound) on the estimated slip rates [*Price and Bürgmann*, 2002]. The design matrix G is constructed for surface displacement and creep data as described by *Harris and Segall* [1987]. The data are weighted so that W contains the available covariance information for each data set. Given the diversity in data used in this analysis, it is also useful to apply a factor α_d that weights the individual data sets relative to one another. A smoothing constraint is imposed using the Laplacian smoothing operator ∇^2, and the relative strength of the smoothing is determined by γ. Since we find that the most northern fault elements are poorly resolved due to the lack of available data north of Point Pinole, a zero slip rate constraint is applied to the most northern fault elements beneath San Pablo Bay. However, we do explore models where this condition is relaxed (see Figure S1 in the auxiliary material).

[16] The choice of how to weight the various data sets is a complicated endeavor given that we are combining a very diverse suite of data types. Assigning a weight would be unnecessary if the full covariances were perfectly known. A similar problem of how to weight diverse data types is encountered in coseismic studies that combine both seismic waveform and geodetic data sets in a kinematic finite source inversion. *Wald and Graves* [2001] assigned comparable overall weights to each data set when they performed a combined waveform and geodetic inversion of synthetic data. Similarly, *Kaverina et al.* [2002] performed a combined inversion for the Hector Mine earthquake. They determined the proper weighting by examining the trade-off in the variance reduction for each data set as a function of weight. Studies that combine multiple geodetic data sets have used various approaches in choosing how to weight the data. Using InSAR and GPS data to examine the Hector Mine earthquake, *Price and Bürgmann* [2002] and *Simons et al.* [2002] chose weights that allow one data set to be fit without substantially degrading the fit to the other data sets. *Jónsson et al.* [2002] used a two-dimensional quantization algorithm to resample the InSAR data based on a variance threshold. They then took the scaled GPS uncertainties and the InSAR uncertainties, and performed an inversion without assigning a weighting factor to either data set.

[17] For this paper, we determined the weight of each data set α_d by plotting the χ^2 normalized by the number of data for each data type as a function of weight (Figure 5). The preferred weight corresponds to the lowest value required to adequately fit the data. The curves in Figure 5 were created by ranging through the weight for one data set while holding the weight fixed to the preferred value for the other data sets. We did not observe a significant degradation of fit to the other data sets during this procedure. In other words, the χ^2 for the three data sets increases by <2% when the weight is varied for the fourth data set. The preferred weights for the InSAR, GPS, surface creep, and CRE data are 0.7, 0.5, 1.0, and 0.6, respectively. The GPS, surface creep and CRE data are strongly sensitive to the respective weighting factor. The InSAR data are less sensitive to weight since the long-wavelength features in the data are fit by a plane. Thus the reduction in χ^2 of the InSAR as the weight is increased reflects the improvement in fit of short-wavelength features in the range change rate.

4. Fault Zone Structure and Geometry

[18] The active surface trace of the Hayward fault is well documented from both geomorphic evidence and from the offset of man-made structures [*Lienkaemper*, 1992]. The fault generally strikes N35°W; however, several salients indicate a more complex fault structure. Starting from the north end of the fault, San Pablo Bay (km −10) resides in an extensional basin formed in a right step over from the Hayward fault to the Rodgers Creek fault [*Parsons et al.*,

Table 3. Slip Rates Determined on the Deep Dislocations for the Preferred Slip Rate Distribution Shown in Figure 7b[a]

Fault	Longitude	Latitude	Longitude	Latitude	Depth, km		Model, mm/yr
					Top	Bottom	
South Calaveras (shallow)	−121.2853	36.6778	−121.7247	37.3555	0	6	17.6 ± 1.9
South Calaveras (deep)	−121.2853	36.6778	−121.7247	37.3555	12	3000	17.6 ± 1.9
North Calaveras	−121.7247	37.3555	−122.0000	37.8012	12	3000	14.6 ± 3.9
Green Valley	−121.9550	37.8500	−199.3447	70.7203	12	3000	7.6 ± 1.4
Greenville	−121.4450	37.4000	−121.8200	37.8500	12	3000	1.6 ± 4.2
Mission	−121.7247	37.3555	−122.0670	37.6760	12	3000	10.0 ± 3.6
Hayward	−122.0670	37.6760	−122.2060	37.8240	12	3000	10.0 ± 3.0
Rodgers Creek	−122.2060	37.8240	−185.0412	64.5061	12	1000	13.7 ± 1.5
Central San Andreas	−95.3344	3.2311	−121.2853	36.6778	12	3000	25.0 ± 6.9
South Bay San Andreas	−121.2853	36.6778	−122.0900	37.2300	12	3000	22.4 ± 1.9
Peninsula San Andreas	−122.0900	37.2300	−122.6733	37.9053	12	3000	14.0 ± 2.6
North San Andreas	−122.6733	37.9053	−158.8147	61.5690	12	3000	18.7 ± 1.1
South San Gregorio	−96.3735	−0.2350	−122.0000	36.5005	12	3000	15.0 ± 6.9
North San Gregorio	−122.0000	36.5005	−122.6733	37.9053	12	3000	0.0 ± 2.8

[a]The coordinates refer to the endpoints of the faults. All faults have a dip of 90°.

2003]. Despite attempts to determine the fault structure below San Pablo Bay using reflection seismology, gravity [*Chapman and Bishop*, 1988], and stratigraphic cross sections [*Wright and Smith*, 1992], a complete description of the fault structure north of Point Pinole (km 0) remains inconclusive. However, it is plausible that the Hayward and Rodgers Creek faults join at depth. Moving south, high-resolution seismic relocations performed by *Waldhauser and Ellsworth* [2002] delineate a subvertical fault plane. Near Berkeley (km 18), seismic clusters illuminate several off-fault, subparallel structures. A diffuse zone of seismicity is observed near Oakland (km 20–30) with no clear organization. A cluster of seismicity beneath San Leandro (km 33) shows a complex fault surface that resembles an inverted flower structure. South of Castro Valley (> km 40), the seismicity at depth and the surface expression of the fault diverge suggesting that the upper few kilometers of the fault dips steeply to the east. The angular offset of the seismicity from the surface trace and the complex nature of the fault surface revealed through the relocations of *Waldhauser and Ellsworth* [2002] suggest that surface displacements are best modeled using a nonplanar surface.

[19] The Hayward fault is represented in our model as an 80 km long by 12 km deep fault plane discretized into 283 triangular subfaults with an average dimension of 3 km. The Hayward fault is meshed in this way in order to accommodate the divergence of the microseismicity at depth and the mapped surface trace as well as to incorporate subsurface salients which may affect the near-fault data. The mesh used in our analysis is provided as auxiliary material. Additional model parameters include fourteen deep, vertical dislocations located beneath the San Gregorio, San Andreas, Mission, Hayward, Rodgers Creek, Calaveras, Green Valley, and Greenville faults. The deep dislocations are used to model the regional strain gradient across the plate boundary. The BVLS approach allows for the right-lateral slip rate to be bound within a range consistent with geologic estimates. All dislocations are bounded between 0 and 40 mm/yr except for the deep Mission and deep Hayward fault dislocations which are fixed at 10 mm/yr. In addition, parallel faults are constrained such that they sum to 40 mm/yr representing the total motion between the Pacific plate and the Sierra Nevada–Great Valley microplate at this latitude [*Argus and Gordon*, 2001].

5. Inversion Results

[20] The slip rates on the deep dislocations are estimated in the inversion and the results for the preferred combined data inversion are shown in Table 3. While these rates agree reasonably well with previously published rates, they are not the focus of this study and only serve the purpose of modeling the regional interseismic deformation field. Generally, the deep slip rates are mostly constrained by the GPS data, but small perturbations of ±1 mm/yr are observed in the slip rates depending on how the various data sets are weighted in a combined data inversion.

[21] The individual contributions from the GPS and InSAR data to the final slip rate distribution on the Hayward fault are evaluated by performing independent inversions. Surface creep data are used in both inversions to constrain slip rate at the top of the fault. Both the InSAR and GPS data sets place slip rate in the top 3–5 km of the fault along its entire length as well as minimal slip rate beneath San Leandro (km 30). The sparse, yet precise nature of the GPS data provide good constraint on the slip rates for the deep faults as discussed above, but provide minimal constraint to the discretized Hayward fault except where a GPS station is close to the surface trace. The GPS data prefer ~5 mm/yr at 8 km depth beneath Berkeley and in the top few kilometers beneath Union City and Hayward (Figure 6a). These locations correlate with regions where an abundance of GPS stations are located near the fault trace. The InSAR data provide better resolution on the shallow Hayward fault due to the dense spatial sampling it provides. Inversions using only the InSAR data prefer >10 mm/yr below Point Pinole (km 0) and ~6 mm/yr beneath Hayward (km 43). The differences of the independent GPS and InSAR derived distributions highlight the limitations of the individual data sets in resolving a low-amplitude signal. The InSAR and GPS data sets are complimentary in that one data set enhances resolution where the other provides inadequate

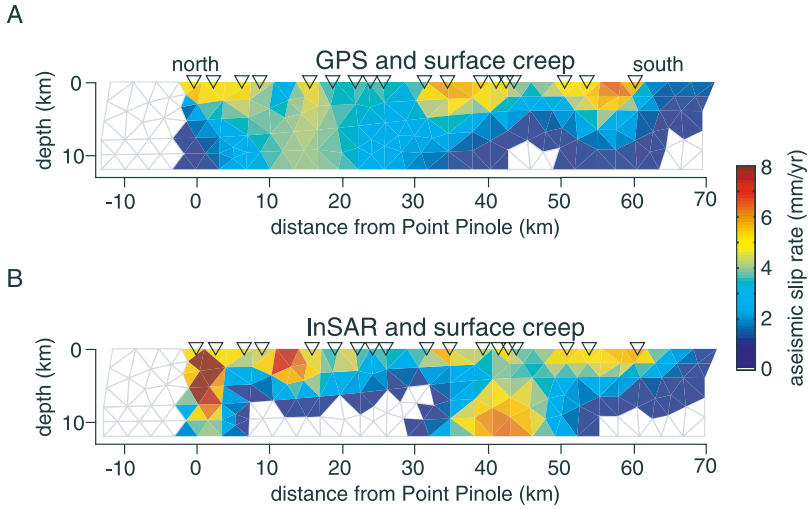

Figure 6. Slip rate distribution using (a) only the GPS data and (b) only the InSAR data establishing the contribution from each data set. Both inversion results also use surface creep rates as a surface constraint (open triangles). InSAR coverage extends along strike from km 0 to km 50. Triangular subfaults with zero inferred slip rate are plotted in white. A zero-slip rate constraint is applied to the most northern subfaults beneath San Pablo Bay.

information and helps to offset any bias that may be contained in any individual data set (see Figure S2 in the auxiliary material for a demonstration). We thus hope to improve the resolution by incorporating a diversity of data.

[22] While the individual slip rate distributions shown in Figure 6 appear disparate, we perform a combined inversion to find the distribution that best satisfies all of the data, including the surface and CRE slip rate estimates. Slip rate distributions are presented for various smoothing weights in Figure 7. An expanded figure detailing how the result of the combined inversion depends on how the data are weighted is provided as Figure S3 in the auxiliary material. We focus our discussion on the slip rate distribution shown in Figure 7b where $\gamma = 1000$ since data misfit increases rapidly for smoother models. A rate of <1 mm/yr is found below San Leandro (km 30) and extends from a depth of ~4 km to the bottom of the fault. The 4 mm/yr rate found adjacent to the Berkeley seismic cluster (km 18) at a depth of ~10 km is largely constrained by the CRE slip rate estimates but is also implied by the GPS data. The inversion places the highest slip rates on the northern portion of the fault beneath Point Pinole (km 0). Directly south of Point Pinole (near km 10) the slip rate at depth abruptly drops to <2 mm/yr.

[23] The fit to the various data sets for the slip rate distribution are shown in Figures 2, 4b, 4c, and 8. The surface creep data and the CRE slip rates are adequately modeled. InSAR residuals are generally less than ±0.5 mm/yr except along the Hayward fault near Point Pinole where residuals are ±1.0 mm/yr. InSAR residuals near Point Pinole are further discussed in section 7.1. Several GPS velocities located directly adjacent to the fault have misfits of 3–5 mm/yr; however, several of these sites represent campaign observations and therefore have large uncertainties. These sites are also located within 100 m of the fault trace and may be susceptible to near-fault complexities. The average GPS residual is 1 mm/yr with most of the residuals pointed in the fault perpendicular direction and no systematic pattern of fault-parallel residuals.

6. Model Resolution

[24] A sensitivity study using synthetic data suggests that the model resolution is spatially variable along the discretized fault due to uneven data coverage. We evaluate the resolution of slip rate by performing repeated inversions of synthetic data where a fault patch with a slip rate of 5 mm/yr is shifted along the fault. The fault patch consists of several adjacent triangular fault elements. For each fault element, the modeled slip rate is then divided by the input slip rate on the asperity to evaluate the ability of the data to resolve the model parameters. The resulting figure shows the percentage of slip rate that we can expect to resolve in the inversion (Figure 9). The resolution for the combined data sets shows that model parameters are well resolved in the top portion of the fault plane and become less resolved below ~6 km, except where CRE estimates are available. At depths greater than 6 km, resolution is improved beneath the town of Hayward (km 55) where the InSAR data are found within one fault depth on both sides of the fault. The portion of the fault beneath San Pablo Bay is less resolved because few data exist to constrain this section.

[25] Several factors complicate the resolution of the model parameters. The InSAR data coverage is asymmetric with inadequate observations on the east side of the fault. Additionally, InSAR data are excluded on the west side of the fault between km 25 and km 30 because of groundwater-induced deformation. This results in poor model resolution because of the sparse data coverage within one fault depth of the surface trace. Similarly, the GPS data are clustered for bench marks directly adjacent to the fault or are otherwise arranged in fault-perpendicular profiles. This results in a nonuniform sampling of the deformation field and can affect the final slip rate distribution. We also

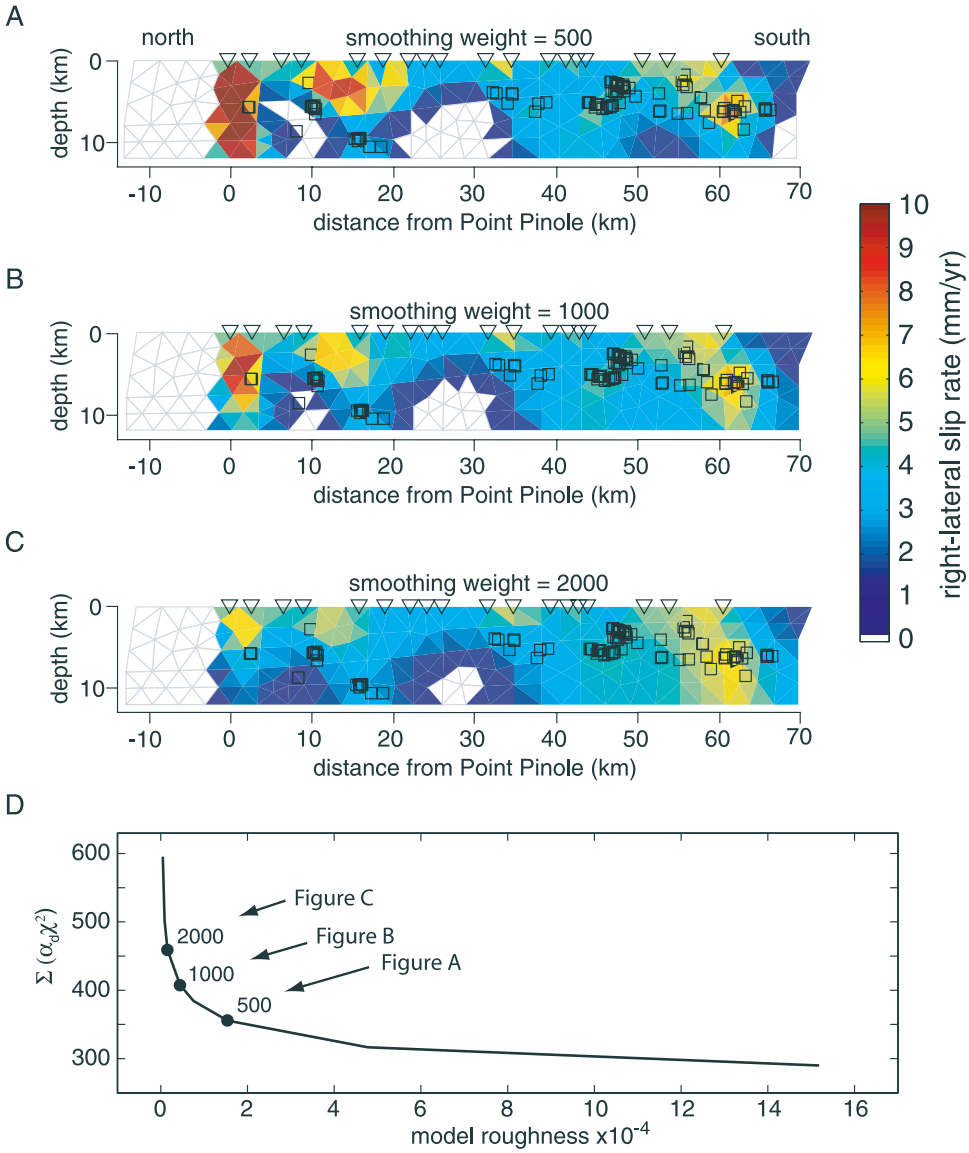

Figure 7. Slip rate distribution on the Hayward fault from a combined inversion of all data. Results for three different smoothing weights are shown: (a) $\gamma = 500$, (b) $\gamma = 1000$, and (c) $\gamma = 2000$. Open triangles and open squares denote the location of surface and CRE-determined slip rates. (d) Choice of smoothing weight for our preferred model ($\gamma = 1000$) determined from the trade-off between the weighted residual sum of squares as measured by $\alpha_d \chi^2$ and the model roughness. Figure S3 in auxiliary material documents how the slip rate distribution varies depending on how the data sets are weighted.

evaluate where the inversion overestimates slip rate in the form of artifacts. This can occur when slip rate is mapped to nearby regions of the fault or the smoothing operator distributes slip rate over a broader surface area. Along-strike slip rate artifacts associated with uneven data coverage did not appear to be a problem, but slip rate is typically smeared along the downdip direction unless the CRE data provide a deeper boundary condition.

7. Discussion

[26] The locations of locked patches inferred in our slip rate distribution are consistent with the locations inferred by previous studies that relied solely on surface creep rates or microseismicity patterns. A slip rate of <1 mm/yr indicates regions where the fault is not slipping either because the fault is locked or because slip is restrained by a nearby asperity. Locked sections may represent the nucleation site or the rupture area of future large earthquakes. We find <1 mm/yr at depth below San Leandro (km 25–35) and potentially below Union City (km 50–60). Either of these low slip rate patches could represent the source region of the 1868 earthquake on the southern Hayward fault and suggest that strain is currently accumulating at depth. A locked patch may also exist below a depth of 8 km near El Cerrito (km 10). The locked patch located at a depth of 5 km near Richmond (km 7) may not be a robust feature due to high slip rate inferred directly to the north and the

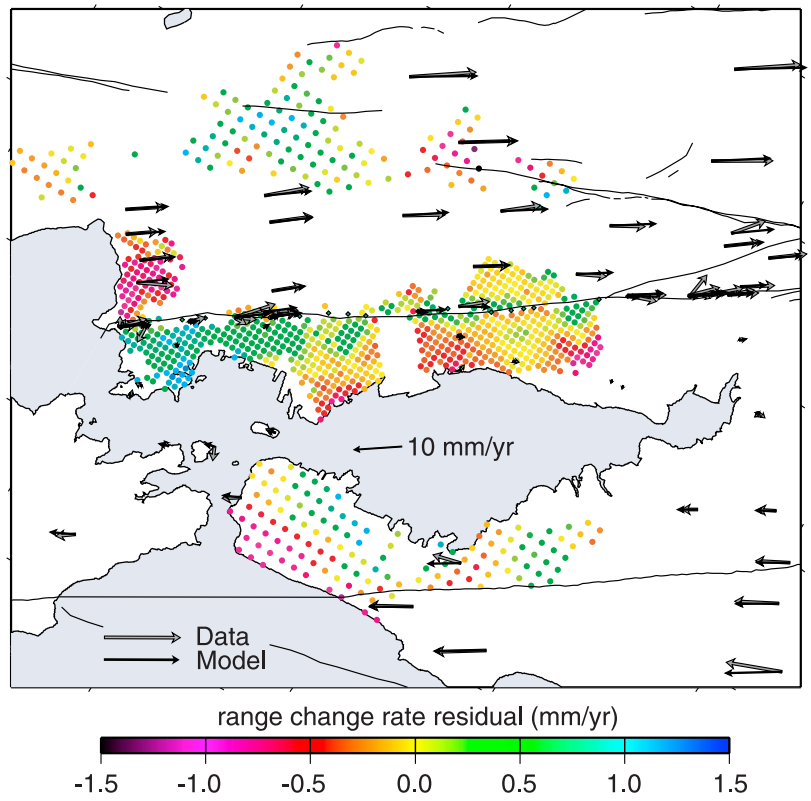

Figure 8. Range change rate residuals (colored dots) between the data and modeled values. GPS data (gray arrows) are compared to the predicted velocities (black arrows) for sites close to the Hayward fault.

uncertainty in how slip rate tapers below San Pablo Bay. *Simpson et al.* [2001] interpreted two local minima in the surface creep rate as evidence for a shallow locking depth beneath San Leandro and Union City. Similarly, *Wyss* [2001] inferred a locked patch beneath San Leandro based on the local recurrence time of seismicity, but was unable to resolve the southern locked patch. *Waldhauser and Ellsworth* [2002] identified potential locked patches based on mircoseismic quiescence and the locations of repeating microearthquakes. They place a locked patch below San Leandro as well as one below Union City. Reduced model resolution at depth below San Leandro raises the issue of whether the <1 mm/yr region reflects a poorly resolved section of the fault or a locked patch. While the maximum slip rate magnitude was poorly resolved at depths greater than 6 km, the inversion of synthetic data was able to detect slip rate on these fault elements. The fact that the inversion of the real data favors nearly zero slip rate beneath San Leandro even when the model is heavily smoothed, suggests that this is a real feature in the final distribution.

7.1. Slip Rate Distribution Beneath Point Pinole

[27] The slip rate distribution presented here differs from previous models with the nearly geologic slip rate inferred on the Hayward fault beneath Point Pinole (km 0). The high slip rate inferred on the northern portion of the fault is strongly driven by the InSAR data. A step function in the range change rate across the fault at Point Pinole is consistent with block-like motion at this location (Figure 10). Additionally, the InSAR data can resolve along-strike variations in the deformation field that reflect slip rate variations at depth. An along-strike increase in range change rate from ~0 to ~2 mm/yr is found along the west side of the fault from Oakland to Point Pinole (Figure 3). This along-strike variation could suggest an increase in the aseismic slip rate at depth as one moves toward Point Pinole. At the fault trace, the InSAR data reveal a 2.2 mm/yr range change offset across the fault which would correspond to 7 mm/yr of right-lateral offset. Surface creep observations suggest a right-lateral slip rate that is 2 mm/yr less than that inferred from InSAR at this location. The InSAR data agree with surface creep rates elsewhere along the fault. In our inversion, the slip rate beneath Point Pinole does not decrease if the zero slip constraint is relaxed on fault elements beneath San Pablo Bay (km <0); instead, the InSAR data prefer >8 mm/yr to extend northward from Point Pinole (see auxiliary material Figure S1). Regardless of how high the slip rates are beneath San Pablo Bay, the nearby GPS data experience only a slight increase in misfit and the surface creep data are accommodated in the inversion by a tapering of the slip rate toward the surface.

[28] The high range change offset across the fault at Point Pinole could indicate a small vertical component that maps into the satellite's line of sight. Approximately 1 mm/yr of range change rate would correspond to 3.2 mm/yr of right-lateral offset or 1.1 mm/yr of east-side-up dip slip. Land subsidence of the region to the west of the fault would increase the range change rate and cause us to overestimate

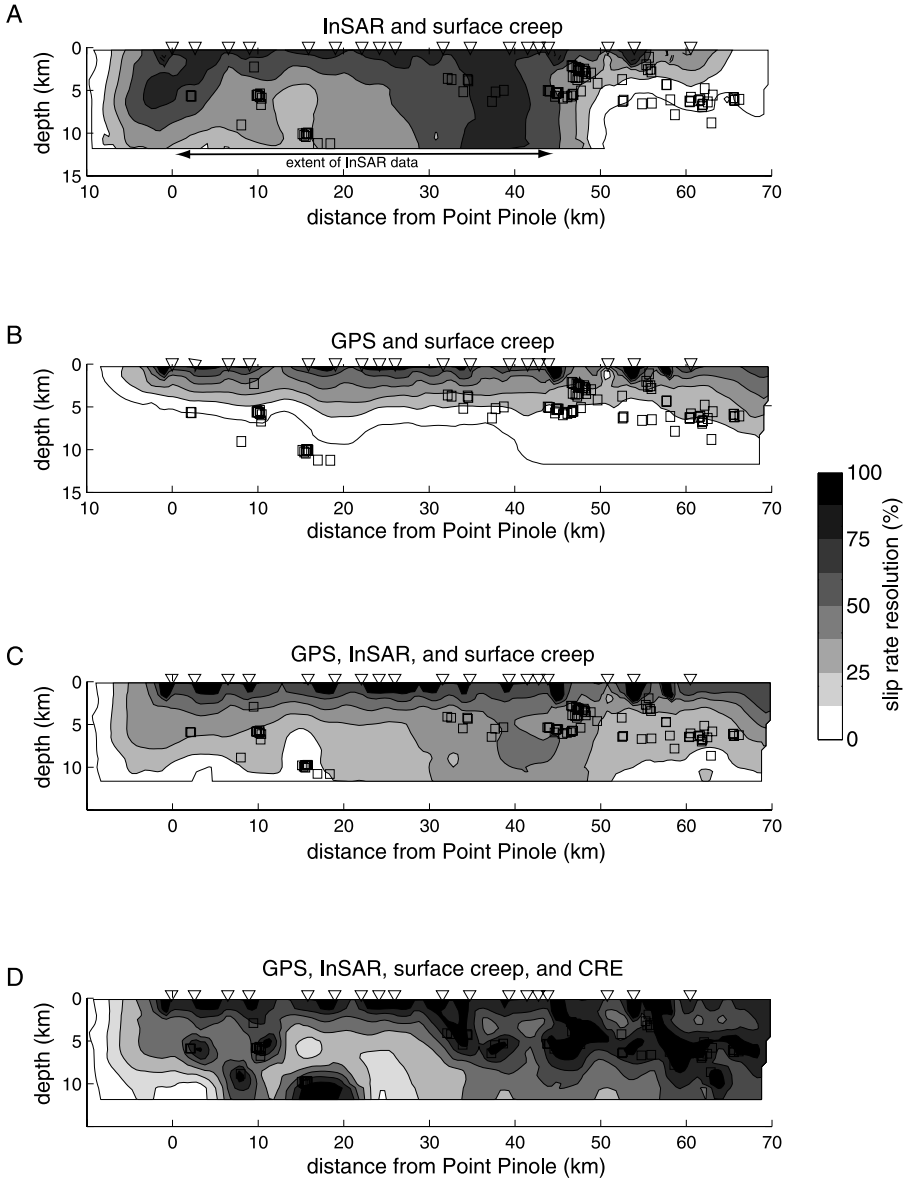

Figure 9. Slip rate resolution on the Hayward fault using (a) InSAR and surface creep, (b) GPS and surface creep, (c) GPS, InSAR, and surface creep data sets, and (d) using all data sets including the CREs. Resolution is evaluated by performing a series of synthetic inversions based on the existing data coverage (see section 6). Slip rate is fully resolved on regions of the fault that have a value of 100%. The contour interval is 12.5%.

the right-lateral creep rate. However, no clear evidence for a long-term land subsidence signal is observed in the 50+ descending interferograms. Ascending InSAR data can be used to constrain any vertical deformation because the SAR data is collected using a different look direction than for a descending SAR geometry. Inspection of three independent ascending interferograms suggests that any vertical deformation at the fault trace must be below the noise level (Figure 10). A fog bank whose eastern advance would be limited by the uplifted hills to the east would also bias the range change observation. The atmospheric water vapor would act to delay the radar signal as it propagates through the atmosphere. SAR data for this region are collected at 11 am local time when the fog has typically retreated to the coast. This would produce a significantly larger standard deviation in the stacked InSAR result because not all of the interferograms would experience this weather. However, fog would not produce the relatively discrete offset in range change at the fault trace, and any atmospheric errors or seasonal deformation is expected to be averaged out in the stack. Even with a slip rate >8 mm/yr below Point Pinole, InSAR data residuals remain high. Therefore we conclude that the InSAR data across Point Pinole can best be explained as a combination of 5–6 mm/yr of right-lateral fault creep and a small vertical component of deformation (east side up) with a rate of $\leq$1 mm/yr.

7.2. Physical Controls on Aseismic Fault Behavior

[29] Aseismic fault behavior has been attributed to a variety of processes and materials. Rate-and-state friction

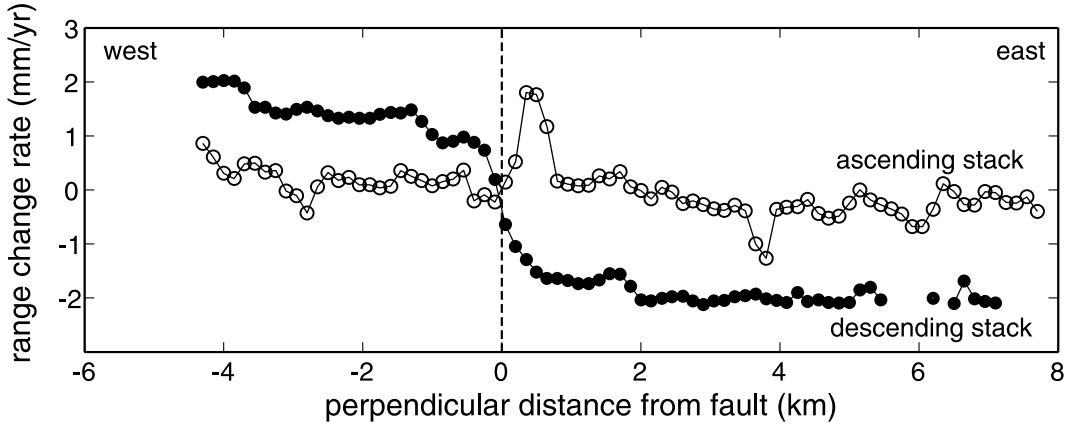

Figure 10. Fault-perpendicular profiles of range change rate across the Hayward fault at Point Pinole. The descending profile is taken along transect A-A′ from the stack of 13 descending interferograms (Figure 3). The ascending profile is taken from a stack of three ascending interferograms (track 478, 19950513 to 19980329, 19960323 to 19990801, and 19960324 to 19991010). The ascending interferograms would show an offset at the fault trace if a significant vertical signal >1 mm/yr were present. For an ascending interferogram, right-lateral creep on the fault and east-side-up signal of ~1 mm/yr would project onto the satellite's line of sight to produce a zero range change rate. The lack of a discrete step in the ascending InSAR data argues that any vertical component on the fault at Point Pinole must be less than 1 mm/yr. The localized jump in range change rate along the ascending profile at x = 0.5 km likely corresponds to an atmospheric artifact in one of the ascending interferograms.

suggests that the stiffness of the surrounding rock and the constitutive properties of the fault surface and gouge zone dictate the slip behavior [*Marone and Scholz*, 1988] where faults with velocity-strengthening conditions exhibit stable creep [*Marone*, 1998]. The presence of clay lithologies or the thickness of the gouge zone are examples of factors that may control the frictional response [*Logan and Rauenzahn*, 1987; *Marone et al.*, 1990]. Alternatively, a heterogeneous stress field imposed on a fault surface [*Rivera and Kanamori*, 2002] could dictate which parts of a fault slip aseismically. Therefore the local stress field could play an important role in determining slip behavior. Since it appears that multiple factors play a role in fault behavior, it is difficult to separate the various effects, such as a heterogeneous stress field versus the frictional properties of the fault zone.

[30] While much work has been done on the individual factors that contribute to aseismic slip, a complete understanding of why certain regions of the Hayward fault are locked and others slip aseismically remains elusive. Improved models of the microseismicity have illuminated the internal structure of the fault zone at depth [*Waldhauser and Ellsworth*, 2002; *Zhang and Thurber*, 2003]. Recent work has also helped to quantify and characterize the fault zone materials [*Moore and Ponce*, 2001; *Ponce et al.*, 2003]. Three-dimensional geologic models of the Hayward fault [*Jachens et al.*, 2003] that assimilate the growing knowledge of the fault zone will help to provide some insight on how the geology correlates with slip behavior. Unfortunately, the uncertainties in our knowledge of both geology and fault behavior at increasing depths will always leave room for ambiguity. However, improved geologic and structural models of the Hayward fault will eventually provide some insight on the first-order controls of fault behavior.

7.3. Seismic Potential

[31] On the basis of the slip rate distribution shown in Figure 7b, we calculate that the Hayward fault is accumulating a slip rate deficit equivalent to a M_w6.77 ± 0.05 per century between km 0 and km 70 assuming a rigidity of 30 GPa and an uncertainty of ±1 mm/yr in the geologic slip rate on the Hayward fault. This estimate of the slip rate deficit is not strongly dependent on the choice of smoothing weight. The strain accumulation rate beneath San Leandro is equivalent to a M_w6.25 event per century, suggesting that this asperity has potentially accumulated enough strain for a M_w6.34 since the 1868 event.

[32] Calculating the potential size of future coseismic events is difficult because we do not fully understand the mode of faulting on faults that exhibit both aseismic and seismic behavior, such as the Hayward fault. As discussed by *Simpson et al.* [2001], it is unknown whether creeping regions of the fault would rupture with the coseismic event or continue to slip aseismically at an accelerated rate. Ultimately we need to better understand the mechanics of the fault to predict how aseismic regions will respond to an abrupt changes in stress.

8. Conclusions

[33] We present the slip rate distribution on the Hayward fault as resolved by surface deformation, characteristic repeating microearthquakes, and surface creep. InSAR data suggest a high slip rate beneath Point Pinole, which may partly be explained by a small component of east-side-up dip slip that projects into the satellite's line of sight. Surface deformation and surface creep rates are consistent with a large locked patch at depth beneath San Leandro. Regions of low slip rate beneath San Leandro and Union City are

potential nucleation sites for future large earthquakes. We estimate an upper bound on the seismic moment accumulation rate to be M_w6.77 per century. However, it is likely that some fraction of this strain will be released in aseismic processes such as afterslip.

Appendix A: InSAR Data Reduction

[34] This section outlines our procedure for selecting an independent set of high-quality interferograms from a large pool of available interferograms. We first considered 37 interferograms all of which have a perpendicular baseline of less than 200 m and a temporal baseline of greater than 1 year. A complete list of interferograms that were processed and considered is given by *Schmidt and Bürgmann* [2003]. The original set of 37 interferograms are stacked by dividing the cumulative range change by the cumulative time spanned which preferentially weights the range change rate of those interferograms with longer temporal baselines. Those interferograms where greater than 5% of the coherent phase exceeds 3 standard deviations from the stacked result are removed from consideration. This eliminates 3 interferograms (all of which have a short temporal baseline) that contain localized atmospheric artifacts with a range change amplitude of 1–2 cm. This procedure provides a level of data quality and ensures that no individual interferogram strongly biases the stack. A subset of 13 interferograms were selected such that no SAR scene is duplicated in any of the interferograms and insures that each interferogram is an independent observation, thus minimizing atmospheric artifacts. The final subset of 13 interferograms used in this analysis is presented in Table 1.

[35] The InSAR data are subsampled in a regular grid with a spacing of 0.75 km between points for regions within 15 km of the Hayward fault. At distances greater than 15 km, the InSAR data are subsampled at a 1.5 km spacing, resulting in a cumulative sampling of 956 points. Each subsampled point represents an average of 9 surrounding pixels in an effort to avoid outliers.

[36] **Acknowledgments.** This work benefited from fruitful discussions with Bob Simpson, Jim Lienkaemper, Roger Bilham, and David Ponce. Constructive reviews were provided by Peter Cervelli, an anonymous reviewer, and the Associate Editor. Poly3D was provided by David Pollard, Stanford University. Andrew Freed created the triangular mesh of the Hayward fault using the software package IDEAS. SAR data were provided to the WInSAR Consortium by the European Space Agency (ESA) through their North American distributor, Eurimage. Original SAR data are copyrighted by ESA (1992–2000). Additional data were provided by an ESA (ENVISAT) data grant. Funding for this work was provided by USGS-NEHRP 03HQGR0069. Berkeley Seismological Laboratory contribution 05-09.

References

Argus, D. F., and R. G. Gordon (2001), Present tectonic motion across the Coast Ranges and San Andreas fault system in central California, *Geol. Soc. Am. Bull.*, *113*, 1580–1592.

Beeler, N. M., D. L. Lockner, and S. H. Hickman (2001), A simple stick-slip and creep-slip model for repeating earthquakes and its implications for microearthquakes at Parkfield, *Bull. Seismol. Soc. Am.*, *91*, 1797–1804.

Bilham, R. (1989), Surface slip subsequent to the 24 November 1987 Superstition Hills, California, earthquake monitored by digital creep meters, *Bull. Seismol. Soc. Am.*, *79*, 424–450.

Bilham, R., and S. Whitehead (1997), Subsurface creep on the Hayward fault, Fremont, California, *Geophys. Res. Lett.*, *24*, 1307–1310.

Bürgmann, R., D. Schmidt, R. M. Nadeau, M. d'Alessio, E. Fielding, D. Manaker, T. V. McEvilly, and M. H. Murray (2000), Earthquake potential along the northern Hayward Fault, California, *Science*, *289*, 1178–1182.

Bürgmann, R., S. Ergintav, P. Segall, E. Hearn, S. McClusky, R. Reilinger, H. Woith, and J. Zschau (2002), Time-dependent distributed afterslip on and deep below the Izmit earthquake rupture, *Bull. Seismol. Soc. Am.*, *91*, 126–137.

Chapman, R. H., and C. C. Bishop (1988), Bouguer gravity map of California: Santa Rosa, 1 × 2-degree sheet, *Reg. Geol. Map Ser. Map 2B*, scale 1:250,000, Calif. Div. Mines and Geol., Sacramento.

Chen, H., and R. Rau (2003), Fault slip rates from repeating microearthquakes on the Chishang fault, eastern Taiwan, *Eos Trans. AGU*, *86*(46), Fall Meet. Suppl., Abstract T11F-06.

Comninou, M., and J. Dundurs (1975), Angular dislocations in a half space, *J. Elast.*, *5*, 203–216.

d'Alessio, M. A., I. A. Johanson, R. Bürgmann, D. A. Schmidt, and M. H. Murray (2005), Slicing up the San Francisco Bay Area: Block kinematics and fault slip rates from GPS-derived surface velocities, *J. Geophys. Res.*, *110*, B06403, doi:10.1029/2004JB003496.

Dragert, H., K. L. Wang, and T. S. James (2001), A silent slip event on the deeper Cascadia subduction interface, *Science*, *292*, 1525–1528.

Galehouse, J. S. (2002), Data from theodolite measurements o f creep rates on San Francisco Bay Region faults, California: 1979–2001, *U.S. Geol. Surv. Open File Rep., 02-225*.

Harris, R. A., and P. Segall (1987), Detection of a locked zone at depth on the Parkfield, California, segment of the San Andreas fault, *J. Geophys. Res.*, *92*, 7945–7962.

Hayward Fault Paleoearthquake Group (1999), Timing of paleoearthquakes on the northern Hayward fault: Preliminary evidence in El Cerrito, California, *U.S. Geol. Surv. Open File Rep., 99-318*.

Herring, T. A. (2002), GLOBK, Global Kalman filter VLBI and GPS analysis program, version 10.0, Mass. Inst. of Technol., Cambridge, Mass.

Igarashi, T., T. Matsuzawa, and A. Hasegawa (2003), Repeating earthquakes and interplate aseismic slip in the northeastern Japan subduction zone, *J. Geophys. Res.*, *108*(B5), 2249, doi:10.1029/2002JB001920.

Jachens, R. C., G. A. Phelps, R. W. Simpson, R. W. Graymer, D. A. Ponce, and C. M. Wentworth (2003), Preliminary insights on Hayward Fault seismicity and geology: Results from analyzing a 3-dimensional geologic map of the Hayward Fault and vicinity, San Francisco Bay Region, California, in *Proceedings of the Hayward Fault Workshop, Eastern San Francisco Bay Area, California, September 19–20, 2003*, edited by D. A. Ponce et al., *U.S. Geol. Surv. Open File Rep., 03-485*, 15–16.

Jónsson, S., H. Zebker, P. Segall, and F. Amelung (2002), Fault slip distribution of the 1999 M_w 7.1 Hector Mine, California, earthquake, estimated from satellite radar and GPS measurements, *Bull. Seismol. Soc. Am.*, *92*, 1377–1389.

Kaverina, A., D. Dreger, and E. Price (2002), The combined inversion of seismic and geodetic data for the source process of the 16 October 1999 M_w 7.1 Hector Mine, California, earthquake, *Bull. Seismol. Soc. Am.*, *92*, 1266–1280.

King, R. W., and Y. Bock (2002), Documentation for the GAMIT GPS Analysis software, release 10.0., Mass. Inst. of Technol., Cambridge, Mass.

Lawson, A. C. (Ed.) (1908), *The California Earthquake of April 18, 1906, Report of the State Earthquake Investigation Commission*, vol. 1, Carnegie Inst. of Washington, Washington, D. C.

Lienkaemper, J. J. (1992), Map of recently active traces of the Hayward fault, Alameda and Contra Costa counties, California, *U.S. Geol. Surv. Map, MF-2196*.

Lienkaemper, J. J., and G. Borchardt (1996), Holocene slip rate on the Hayward fault at Union City, California, *J. Geophys. Res.*, *101*, 6099–6108.

Lienkaemper, J. J., and J. Galehouse (1997), Revised long-term creep rates on the Hayward fault, Alameda and Contra Costa counties, California, *U.S. Geol. Surv. Open File Rep., 97-690*.

Lienkaemper, J. J., and J. Galehouse (1998), New evidence doubles the seismic potential of the Hayward fault, *Seismol. Res. Lett.*, *69*, 519–523.

Lienkaemper, J. J., and P. L. Williams (1999), Evidence for surface rupture in 1868 on the Hayward fault in north Oakland and major rupturing in prehistoric earthquakes, *Geophys. Res. Lett.*, *26*, 1949–1952.

Lienkaemper, J. J., G. Borchardt, and M. Lisowski (1991), Historic creep rate and potential for seismic slip along the Hayward fault, California, *J. Geophys. Res.*, *96*, 18,261–18,283.

Lienkaemper, J. J., J. S. Galehouse, and R. W. Simpson (1997), Creep response of the Hayward Fault to stress changes caused by the Loma Prieta earthquake, *Science*, *276*, 2014–2016.

Lienkaemper, J. J., J. S. Galehouse, and R. W. Simpson (2001), Long-term monitoring of creep rate along the Hayward fault and evidence for a lasting creep response to 1989 Loma Prieta earthquake, *Geophys. Res. Lett.*, *28*, 2265–2268.

Linde, A. T., M. T. Gladwin, M. J. S. Johnston, and R. L. Gwyther (1996), A slow earthquake sequence on the San Andreas fault, *Nature*, *383*, 65–68.

Logan, J. M., and K. A. Rauenzahn (1987), Frictional dependence of gouge mixtures of quartz and montmorillonite on velocity, composition and fabric, *Tectonophysics*, *144*, 87–108.

Malservisi, R., C. Gans, and K. P. Furlong (2003), Numerical modeling of creeping faults and implications for the Hayward fault, California, *Tectonophysics*, *361*, 121–137.

Marlow, M. S., R. C. Jachens, P. E. Hart, P. R. Carlson, R. J. Anima, and J. R. Childs (1999), Development of San Leandro synform and neotectonics of the San Francisco Bay block, California, *Mar. Pet. Geol.*, *16*, 431–442.

Marone, C. (1998), Laboratory-derived friction laws and their application to seismic faulting, *Annu. Rev. Earth Planet. Sci.*, *26*, 643–696.

Marone, C., and C. H. Scholz (1988), The depth of seismic faulting and the upper transition from stable to unstable slip regimes, *Geophys. Res. Lett.*, *15*, 621–624.

Marone, C., C. B. Raleigh, and C. H. Scholz (1990), Frictional behavior and constitutive modeling of simulated fault gouge, *J. Geophys. Res.*, *95*, 7007–7025.

Miller, M. M., T. Melbourne, D. J. Johnson, and W. Q. Sumner (2002), Periodic slow earthquakes from the Cascadia subduction zone, *Science*, *295*, 2423.

Moore, D. E., and D. A. Ponce (2001), Petrography and physical properties of selected rock types associated with the Hayward fault, California, *U.S. Geol. Surv. Open File Rep., 01-263*.

Nadeau, R. M., and L. R. Johnson (1998), Seismological studies at Parkfield. VI: Moment release rates and estimates of source parameters for small repeating earthquakes, *Bull. Seismol. Soc. Am.*, *88*, 790–814.

Nadeau, R. M., and T. V. McEvilly (1999), Fault slip rates at depth from recurrence intervals of repeating microearthquakes, *Science*, *285*, 718–721.

Nadeau, R. M., and T. V. McEvilly (2004), Periodic pulsing of characteristic microearthquakes on the San Andreas fault, *Science*, *303*, 220–222.

Nadeau, R. M., W. Foxall, and T. V. McEvilly (1995), Clustering and periodic recurrence of microearthquakes on the San Andreas fault at Parkfield, California, *Science*, *267*, 503–507.

Okada, Y. (1985), Surface deformation due to shear and tensile faults in a half-space, *Bull. Seismol. Soc. Am.*, *75*, 1135–1154.

Oppenheimer, D. H., I. G. Wong, and F. W. Klein (1992), The seismicity of the Hayward fault, California, in *Proceedings of the second conference on earthquake hazards in the eastern San Francisco Bay Area*, G. Borchardt et al., *Spec. Publ. Calif. Div. Mines Geol.*, *113*, 91–100.

Parsons, T., R. Sliter, E. L. Geist, R. C. Jachens, B. E. Jaffe, A. Foxgrover, P. E. Hart, and J. McCarthy (2003), Structure and Mechanics of the Hayward-Rodgers Creek fault step-over, San Francisco Bay, California, *Bull. Seismol. Soc. Am.*, *93*, 2187–2200.

Ponce, D. A., T. G. Hildenbrand, and R. C. Jachens (2003), Gravity and magnetic expression of the San Leandro gabbro with implications for the geometry and evolution of the Hayward fault zone, northern California, *Bull. Seismol. Soc. Am.*, *93*, 14–26.

Price, E. J., and R. Bürgmann (2002), Interactions between the Landers and Hector Mine, California, earthquakes from space geodesy, boundary element modeling, and time-dependent friction, *Bull. Seismol. Soc. Am.*, *92*, 1450–1469.

Rivera, L., and H. Kanamori (2002), Spatial heterogeneity of tectonic stress and friction in the crust, *Geophys. Res. Lett.*, *29*(6), 1088, doi:10.1029/2001GL013803.

Sammis, C. G., and J. R. Rice (2001), Repeating earthquakes as low-stress-drop events at a border between locked and creeping fault patches, *Bull. Seismol. Soc. Am.*, *91*, 532–537.

Savage, J. C., and M. Lisowski (1993), Inferred depth of creep on the Hayward fault, central California, *J. Geophys. Res.*, *98*, 787–793.

Schmidt, D. A. (2002), The kinematics of faults in the San Francisco Bay Area inferred from geodetic and seismic data, Ph.D. thesis, 181 pp., Univ. of Calif., Berkeley.

Schmidt, D. A., and R. Bürgmann (2003), Time-dependent land uplift and subsidence in the Santa Clara valley, California, from a large interferometric synthetic aperture radar data set, *J. Geophys. Res.*, *108*(B9), 2416, doi:10.1029/2002JB002267.

Simons, M., Y. Fialko, and L. Rivera (2002), Coseismic deformation from the 1999 M_w 7.1 Hector Mine, California, earthquake as inferred from InSAR and GPS observations, *Bull. Seismol. Soc. Am.*, *92*, 1390–1402.

Simpson, R. W., J. J. Lienkaemper, and J. S. Galehouse (2001), Variations in creep rate along the Hayward fault, California, interpreted as changes in depth of creep, *Geophys. Res. Lett.*, *28*, 2269–2272.

Smith, S. W., and M. Wyss (1968), Displacement on the San Andreas fault subsequent to the 1966 Parkfield earthquake, *Bull. Seismol. Soc. Am.*, *58*, 1955–1973.

Stark, P. B., and R. L. Parker (1995), Bounded variable least squares: An algorithm and applications, *J. Comp. Stat.*, *10*, 129–141.

Templeton, D. C., R. M. Nadeau, and R. Bürgmann (2001), Structure and kinematics at the juncture between the San Andreas and southern Calaveras faults, *Eos Trans. AGU*, *82*(47), Fall Meet. Suppl., Abstract S32E-02.

Thomas, A. L. (1993), Poly3D: A three-dimensional, polygonal element, displacement discontinuity boundary element computer program with applications to fractures, faults, and cavities in the earth's crust, Masters thesis, 221 pp., Stanford Univ., Stanford, Calif.

Toppozada, T. R., and G. Borchardt (1998), Re-evaluation of the 1836 'Hayward fault' earthquake and the 1838 San Andreas fault earthquake, *Bull. Seismol. Soc. Am.*, *88*, 140–159.

Wald, D. J., and R. W. Graves (2001), Resolution analysis of finite fault source inversion using one- and three-dimensional Green's functions: 2. Combining seismic and geodetic data, *J. Geophys. Res.*, *106*, 8767–8788.

Waldhauser, F., and W. L. Ellsworth (2002), Fault structure and mechanics of the Hayward Fault, California, from double-difference earthquake locations, *J. Geophys. Res.*, *107*(B3), 2054, doi:10.1029/2000JB000084.

Wesson, R. L. (1988), Dynamics of fault creep, *J. Geophys. Res.*, *93*, 8929–8951.

Williams, P. L. (1995), Features and dimensions of the Hayward fault zone in the Strawberry and Blackberry creek area, Berkeley, California, *Publ. 36852*, Lawrence Berkeley Natl. Lab., Berkeley, Calif.

Working Group on California Earthquake Probabilities (2003), Earthquake probabilities in the San Francisco Bay region: 2002 to 2031, *U.S. Geol. Surv. Open File Rep., 03-214*.

Wright, T. L., and N. Smith (1992), Right step from the Hayward fault to the Rodgers Creek fault beneath San Pablo bay, in *Proceedings of the second conference on earthquake hazards in the eastern San Francisco Bay Area*, G. Borchardt et al., *Spec. Publ. Calif. Div. Mines Geol.*, *113*, 407–417.

Wyss, M. (2001), Locked and creeping patches along the Hayward fault, California, *Geophys. Res. Lett.*, *28*, 3537–3540.

Yu, E., and P. Segall (1996), Slip in the 1868 Hayward earthquake from the analysis of historical triangulation data, *J. Geophys. Res.*, *101*, 16,101–16,118.

Zhang, H. J., and C. H. Thurber (2003), Double-difference tomography: The method and its application to the Hayward fault, California, *Bull. Seismol. Soc. Am.*, *93*, 1875–1889.

R. Bürgmann, Department of Earth and Planetary Science, 307 McCone Hall, University of California, Berkeley, CA 94720-4767, USA. (burgmann@seismo.berkeley.edu)

M. d'Alessio, U.S. Geological Survey, 345 Middlefield Rd., MS 977, Menlo Park, CA 94025, USA. (dalessio@usgs.gov)

R. M. Nadeau, Berkeley Seismological Laboratory, 211 McCone Hall, University of California, Berkeley, CA 94720-4760, USA. (nadeau@seismo.berkeley.edu)

D. A. Schmidt, Department of Geological Sciences, 1272 University of Oregon, Eugene, OR 97403-1272, USA. (das@uoregon.edu)